



Experimental and theoretical studies on MEMS piezoelectric vibrational energy harvesters with mass loading

Robert Andosca^{a,b}, T. Gus McDonald^b, Vincent Genova^c, Steven Rosenberg^b, Joseph Keating^d, Cole Benedixen^d, Junru Wu^{a,b,*}

^a Department of Physics and Materials Science Program, University of Vermont, Burlington, VT 05405 United States

^b MicroGen Systems, Inc., Cornell Business & Technology Park, Ithaca, NY 14850 United States

^c Cornell NanoScale Science and Technology Facility, Cornell University, Ithaca, NY 14850 United States

^d Infinite Power Solutions, Inc., Littleton CO, 80127 United States

ARTICLE INFO

Article history:

Received 16 October 2011

Received in revised form 14 February 2012

Accepted 20 February 2012

Available online 28 February 2012

Keywords:

Piezoelectric

Vibrational energy

Harvesters

Scavengers

MicroElectroMechanical systems

MEMS devices

ABSTRACT

Experimental and theoretical investigations on micro-scale multi-morph cantilever piezoelectric vibrational energy harvesters (PZEHs) of the MicroElectroMechanical Systems (MEMS) are presented. The core body of a PZEH is a “multi-morph” cantilever, where one end is clamped to a base and the other end is free. This “fixed-free” cantilever system including a proof-mass (also called the end-mass) on the free-end that can oscillate with the multi-layer cantilever under continuous sinusoidal excitations of the base motion. A partial differential equation (PDE) describing the flexural wave propagating in the multi-morph cantilever is reviewed. The resonance frequencies of the lowest mode of a multi-morph cantilever PZEH for some ratios of the proof-mass to cantilever mass are calculated by either solving the PDE numerically or using a lumped-element model as a damped simple harmonic oscillator; their results are in good agreement (disparity $\leq 0.5\%$). Experimentally, MEMS PZEHs were constructed using the standard micro-fabrication technique. Calculated fundamental resonance frequencies, output electric voltage amplitude V and output power amplitude P with an optimum load compared favorably with their corresponding measured values; the differences are all less than 4%. Furthermore, a MEMS PZEH prototype was shown resonating at 58.0 ± 2.0 Hz under 0.7 g ($g = 9.81$ m/s²) external excitations, corresponding peak power reaches 63 μ W with an output load impedance Z of 85 k Ω . This micro-power generator enabled successfully a wireless sensor node with the integrated sensor, radio frequency (RF) radio, power management electronics, and an advanced thin-film lithium-ion rechargeable battery for power storage at the 2011 Sensors Expo and Conference held in Chicago, IL. In addition, at 58 Hz and 0.5, 1.0 g excitations power levels of 32, and 128 μ W were also obtained, and all these three power levels demonstrated to be proportional to the square of the acceleration amplitude as predicted by the theory. The reported P at the fundamental resonance frequency f_1 and acceleration G -level, reached the highest “Figure of Merit” [power density \times (bandwidth/resonant frequency)] achieved amongst those reported in the up-to-date literature for high quality factor Q_f MEMS PZEH devices.

© 2012 Elsevier B.V. All rights reserved.

1. Introduction

Wireless sensor networks (WSNs) are foreseen to become widespread as an inevitable “third wave of computing revolution” [1–3]. Experts of the WSN industry envisage that many thousands of wireless micro-sensors will be distributed in near future as a network or “web” throughout our environment such as a city, a country, or even multi-countries. Relatively small scale sensors

could be installed in automobiles, aircraft, trains, buildings, factories, city blocks, and many others [4–9]. Wireless sensors distributed in a network would collect data and send back the information to a central hub for processing. This vision is referred to “ambient intelligence” or “pervasive computing” [10–12]. WSN nodes will need to be powered autonomously. To be truly “wireless” these devices will become “cordless”, which in the end will be the most cost effective by neither having to re-wire a building nor constantly replace batteries.

Today most wireless sensor nodes are powered by batteries. The battery life cycle is typically between three (3) months and three (3) years depending upon duty cycle of applications [12]. The extensive periodic replacement of these batteries in a WSN is labor-intensive and time consuming. It could also cause a multitude

* Corresponding author at: Professor of Physics Department and Materials Science Program, University of Vermont, Dept. of Physics, Cook Bldg., University of Vermont, Burlington, VT 05405, USA. Tel.: +1 802 656 8357; fax: +1 802 656 0817.

E-mail address: jwu@uvm.edu (J. Wu).

Nomenclature

ω_n	n th resonance angular frequency in X - Z -plane
f_n	n th resonance frequency of bending modes in X - Z plane
E_i	Young's modulus of i th layer in multi-morph
I	the cross-sectional area moment of inertia
A_i	cross-sectional area of i th layer in multi-morph
C	bending curvature
R	radius of curvature
L	cantilever length
d_{ij}	piezoelectric coupling coefficient matrix
K_p	dielectric constant of piezoelectric material
k	dimensionless coupling coefficient
$z(x,t)$	displacement in z -direction
z_0	displacement amplitude of input excitation
$f(t)$	linear force per unit length in z -direction
G	acceleration amplitude
g	acceleration due to gravity
$m = \rho A$	linear mass density
ρ_i	density of i th layer material
b_m	resistance force coefficient
$\beta_n = b_m/2m\omega_n$	n th mode damping coefficient per linear mass
k_n	wave-number of a bending wave propagating in X - Z -plane (n th mode).
D	electrical field displacement vector, where $D_1 = D_x$, $D_2 = D_y$ and $D_3 = D_z$
d_{31}	electrical polarization z -direction coupling coefficient due to stress/strain in x -direction
d_{32}	electrical polarization z -direction coupling coefficient due to stress/strain in y -direction
d_{33}	electrical polarization z -direction coupling coefficient due to stress/strain in z -direction
E_p	Young's modulus of the piezoelectric material
ϵ_{11}	strain in a plane having x -direction as the normal direction due to force in x -direction
ϵ_{22}	strain in a plane having y -direction as the normal due to force in y -direction
ϵ_{33}	strain in a plane having z -direction as the normal due to force in z -direction
τ_{23}	shear stress in a plane having y -direction as the normal due to force in z -direction
τ_{13}	shear stress in a plane having x -direction as the normal direction due to force in z -direction
τ_{12}	shear stress in a plane having x -direction as the normal due to force in y -direction
R	radius of curvature in XZ -plane
Z_N	torque neutral axes in z -direction
Z_p	axes measured from an arbitrary reference to the center of area of the piezoelectric layer in the z -direction
Z_i	axes measured from an arbitrary reference to the center of i th layer in the z -direction
Q	charge
$C_p = \epsilon_0 K_p wL/t_p$	capacitance across piezoelectric material
t_p	piezoelectric material thickness
t_i	i th layer thickness
ϵ_0	permittivity of free space
K_p	piezoelectric material dielectric constant
$\delta_{1,\max}$	the maximum deflection of the beam in the z -direction for the first mode
$V_{1,\max}$	voltage amplitude when $\omega = \omega_1$
$R_i = Z$	optimal resistance for max power output

V	output voltage
V_p	peak V
P	output power
P_p	peak P

of exhausted batteries to end up in landfills generating an environmental disaster. A technology that is being researched today is "power scavenging" or "energy harvesting", which intends to replace or extend the lifespan of batteries for wireless sensor and WSN applications. There are several forms of small to large scale energy harvesters that exist today, which include electromagnetic, photovoltaic (solar), radio frequency (RF), thermal, water turbines, and wind power. There are *meso*-scale and MEMS versions of these devices either in practice or under development [13–16]. Yet, for some applications these types of energy sources are not practical in many environments, such as inside an automobile tire, under a bridge, embedded in concrete, in a heating system, ventilation, and air condition (HVAC) ductwork, and other places which are hard to reach due to harsh environmental conditions. Hence, an alternative energy supply is needed.

Ambient mechanical vibration is another source of energy that could be taken advantage of for many applications in their associated environments. There are three typical ways to scavenge energy from vibration, (1) electromagnetic (e.g. moving inductive coil with a fixed permanent magnet, or vice versa), (2) electrostatic (e.g. capacitive MEMS "comb-drive"), which works like an accelerometer, yet instead of measuring changes in capacitance it generates an alternating change in charge per unit time, or power, and (3) piezoelectric. Roundy et al. [4] has discussed these vibrational energy harvesters in detail. It was stated that electromagnetic sources cannot produce enough voltage due to typical electromagnetic scaling issues, and electrostatic devices need an external voltage source, that is contrary to the autonomous principle of power sources. In the end, it was shown that PZEH devices have the highest energy density and may produce voltages between 1–20V, enough to be utilized by a wireless sensor node with power management circuitry and storage (e.g. advanced thin-film rechargeable batteries and/or ultra-capacitors). In addition, power densities greater than $100 \mu\text{W}/\text{cm}^3$ have been claimed to be achievable.

A cantilever-type power generator is the focus of this study; one end of the cantilever is clamped to a base and the other free-end may be attached with a mass of M . There have been several studies of this type of fixed-free cantilever with and without mass loading M . *Meso*-scale (mechanically assembled devices) PZEH devices with resonant frequencies in the range of 100–200 Hz with power levels up to $375 \mu\text{W}/\text{cm}^3$ were produced by Roundy and his colleagues [4]; the cost to produce these *meso*-devices was estimated to be on the order of several hundred dollars. And, since these are manually or mechanically assembled, it will be difficult to reduce the production cost even in high volume. One way to reduce the cost level would be developing MEMS PZEH devices employing micro-fabrication (batch) techniques on standard silicon (Si) substrates. The cost will continue to drop with increasing fabrication volume, just like computer-chips [17]. It is estimated that a single MEMS PZEH die production cost (including wafer-scale-packaging; WSP) will be less than \$1 to \$10 each depending upon the die size ($<1 \text{ cm} \times 1 \text{ cm}$) and wafer diameter when it is volume manufactured.

Other researchers [7,8,13,16] have demonstrated feasibility of MEMS-based PZEH devices; the frequency range was mostly above 400 Hz. However, in a survey by Roundy et al. [4]; it was reported that most ambient vibrations (automobiles, building's HVAC ducts, microwave ovens, and others) have resonance frequency

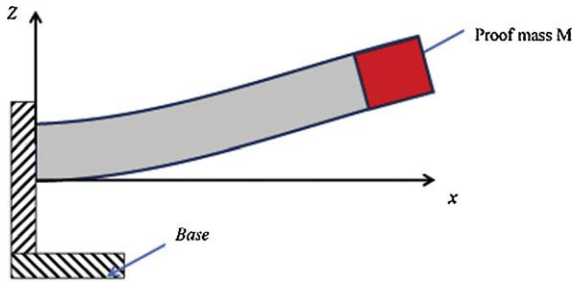


Fig. 1. Illustration of a single cantilever with a proof mass.

of 132 ± 84 Hz. It is the intention of the authors to gear PZEH designs model towards these low frequencies to meet the wide demand [12].

In terms of mathematical modeling of a single cantilever vibrator, the lumped element (mass-spring-dashpot) model has been often used [10]. The distributed-parameter systems are also used in modeling [7,18,19] the flexural wave propagations. Chen et al. [7] modeled the bending mode of a bi-morphs piezoelectric harvester without a proof mass and they also derived analytical solutions. Erturk and Inman [18] did extensive mathematic study on a distributed parameter electromechanical model for a unimorph-cantilevered piezoelectric energy harvester. In addition to the vertical oscillations of the base as the excitation, they also included the effect due to its small rotation. Up to the authors' knowledge, there has been no report on a detailed mathematical analysis combined with the experimental confirmation on a multi-morph cantilever PZEH with the mass loading.

2. Theory

2.1. Review of fundamental mechanics of flexural mode of a beam

The flexural (bending) wave excitation of a single beam will be the focus of this section. At one end ($x=0$) it is clamped to a base and at the other end, it is attached with a proof-mass M of dimensions much smaller than the beam length as shown in Fig. 1.

Meirovitch [19] derived the following PDE for the single beam based on the principle of virtual work by D'Alembert [22]

$$EI \frac{\partial^4 z(x, t)}{\partial x^4} + m \frac{\partial^2 z(x, t)}{\partial t^2} - F(x, t) = 0 \quad (0 < x < L), \quad (1)$$

where $z(x, t)$ is the relative displacement of the cantilever with respect to the base, subject to the following boundary conditions

$$\text{at } z = 0 : z(0, t) = 0 \text{ and } \frac{\partial z(0, t)}{\partial x} = 0; \quad (2)$$

at $x=L$ (neglecting the dimension of the proof mass):

$$EI \frac{\partial^2 z(x, t)}{\partial x^2} = 0, \quad (3)$$

and

$$EI \frac{\partial^3 z(x, t)}{\partial x^3} - M \frac{\partial^2 z(L, t)}{\partial t^2} = 0; \quad (4)$$

where E is the elastic modulus, m is the mass per unit length of the beam, I is the cross-sectional area moment of inertia about the central axis of the beam. The product of E and I , EI is called the flexural rigidity [20], and $F(x, t)$ includes the damping and external driving forces due to the sinusoidal excitations of the base motion.

2.2. Multi-morph cantilevers

A fixed-free cantilever comprises of multiple thin material film layers of length L , width W and thickness t_i attached with a mass

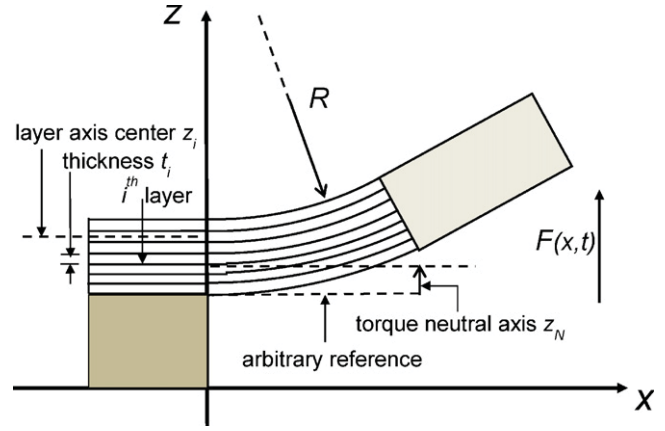


Fig. 2. Illustration of a "multi-morph" cantilever, and the coordinate system applied. Used for mathematical derivation.

M at the free end ($x=L$) and the other end is clamped ($x=0$), where one layer is of a piezoelectric material and the others are purely elastic. Weinberg, and Chen et al. use the "multi-morph" structure to physically and mathematically describe piezoelectric actuators/MEMS-based PZEHs [7,20]. This paper uses the same representation to describe the physical situation depicted in Fig. 2. The thin-film layer interfaces are smooth and continuous and do not slip with respect to each other. It is assumed that all layers are uniform in nature, where Young's modulus E_i , rotational inertial I_i , thickness t_i , and cross-sectional areas $A_i (= Wt_i)$; the subscript i denotes the i th specific layer. The bending induced curvature $C = 1/R$ (Fig. 2) and the piezoelectric effect, i.e., the dimensionless coupling coefficient $k = (d_{31}^2 E_p / \epsilon_0 K_p)^{1/2}$ are assumed to be much smaller than $1/L$ and unity respectively, where d_{31} , E_p , ϵ_0 , and K_p are electrical polarization along z -direction coupling coefficient due to stress/strain in x -direction, Young's modulus, permittivity of free space and dielectric constant of the piezoelectric material respectively.

The flexural rigidity about the neutral axis located at z_N (Fig. 2) is given by

$$\begin{aligned} EI &= \sum_{i=1}^N \left\{ A_i E_i \left[\left((z_i - z_N)^2 + \frac{t_i^2}{12} \right) \right] \right\} \\ &= \sum_{i=1}^N \left\{ W t_i E_i \left[\left((z_i - z_N)^2 + \frac{t_i^2}{12} \right) \right] \right\}, \end{aligned} \quad (5)$$

where $z_N = \sum_{i=1}^N E_i t_i z_i / \sum_{i=1}^N E_i t_i$ and z_i is the location of the axis of the i th layer with respect to an arbitrary reference. Thus in Eq. (1),

$$m = \sum_{i=1}^N \rho_i W t_i, \quad (6)$$

$$F(x, t) = -b_m \frac{\partial z(x, t)}{\partial t} - F(t). \quad (7)$$

here the first term on the right side of Eq. (7) is the damping resistant force including both transduction damping and parasitic damping, and the second term $F(t)$ is the force applied to the beam due to the vibration of the base along vertical (z) direction and $z(x, t)$ is the instant vertical deflection, and the base rotation effect is neglected. Thus, Eq. (1) can be rewritten as

$$EI \frac{\partial^4 z(x, t)}{\partial x^4} + m \frac{\partial^2 z(L, t)}{\partial t^2} + b_m \frac{\partial}{\partial t} [z(x, t)] = F(t). \quad (8)$$

Letting $F(t) = 0$ in Eq. (8), it becomes the corresponding homogeneous PDE, which can be solved using the separation variable

technique [7,21]. The general solutions may be expressed as $z(x, t) = \sum_{n=1}^{\infty} Y_n(x)T_n(t)$, where

$$\frac{d^4 Y_n(x)}{dx^4} - k_n^4 Y(x) = 0, \tag{9}$$

$$\sum_{n=1}^{\infty} \left\{ Y_n(x) \left[\frac{d^2 T_n(t)}{dt^2} + 2\beta_n \omega_n \frac{dT_n(t)}{dt} + \omega_n^2 T_n(t) \right] \right\} = f(t), \tag{10}$$

$$2\beta_n \omega_n = b_m/m, \text{El}k_n^4/m = \omega_n^2 \text{ and } f(t) = F(t)/m.$$

The following boundary conditions, at $x=0$, $Z(0) = [dZ(x)/dx]_{x=0} = 0$ and at $x=L$:

$$EI \frac{\partial^2 z(x, t)}{\partial x^2} = 0, \tag{11}$$

and

$$EI \frac{\partial^3 z(x, t)}{\partial x^3} - M \frac{\partial^2 z(x, t)}{\partial t^2} = 0 \tag{12}$$

need to be satisfied.

After satisfying the aforementioned boundary conditions (Eqs. (11) and (12)), the spatial parts of the solutions may be obtained as

$$Y_n(x) = C_1 \left\{ [\cos(k_n x) - \cos h(k_n x)] - \frac{\cos(k_n L) + \cos h(k_n L)}{\sin(k_n L) + \sin h(k_n L)} \times [\sin(k_n x) - \sin h(k_n x)] \right\}, \tag{13}$$

where the values of k_n are determined by numerical calculations, which in general is mass loading M dependent. For a special case, if there is no mass attached, i.e., $M=0$, the eigenvalues k_n can be determined by

$$\cos(k_n L) \cos h(k_n L) = -1, \quad n = 1, 2, 3 \dots \tag{14}$$

Thus Eq. (14) can be solved numerically; the resulting eigenvalues are $\xi_1 = k_1 L = 1.8751$, $\xi_2 = k_2 L = 4.6941$, $\xi_3 = k_3 L = 7.8548$, etc. Note that the ratios of eigenvalues are not integers; a characteristic of flexural waves [21]. The corresponding eigenfunctions are orthogonal with each other in this case ($M=0$) [7,18].

Now we come back to the non-homogeneous Eq. (8), and focus on its particular solution of the lowest mode ($n=1$) which is most relevant to a MEMS-based PZEH.

If the driving force is caused by a sinusoidal continuous displacement $z_0 e^{-i\omega_1 t}$ of the base where the cantilever is attached, then the driving force per unit length is given by

$$f(t) = \frac{F(t)}{m} = \frac{d^2(z_0 e^{-i\omega_1 t})}{dt^2} = -z_0 \omega_1^2 e^{-i\omega_1 t}. \tag{15}$$

From Eq. (10), one obtains

$$Y_1(x)[\ddot{T}_1(t) + 2\beta_1 \omega_1 \dot{T}_1(t) + \omega_1^2 T_1(t)] = -z_0 \omega_1^2 e^{-i\omega_1 t}. \tag{16}$$

Multiplying both sides by $Y_1(x)$

$$[Y_1(x)]^2 [\ddot{T}_1(t) + 2\beta_1 \omega_1 \dot{T}_1(t) + \omega_1^2 T_1(t)] = -Y_1(x)[z_0 \omega_1^2 e^{-i\omega_1 t}] \tag{17}$$

Rearranging and integrating Eq. (17), one obtains

$$\begin{aligned} \ddot{T}_1(t) + 2\beta_1 \omega_1 \dot{T}_1(t) + \omega_1^2 T_1(t) &= \frac{-\int_0^L Y_1(x) dx}{\int_0^L Y_1^2(x) dx} z_0 \omega_1^2 e^{-i\omega t} \\ &= -A_1(L) z_0 \omega_1^2 e^{-i\omega_1 t}, \end{aligned} \tag{18}$$

$$\text{where } A_1(L) = \frac{-\int_0^L Y_1(x) dx}{\int_0^L Y_1^2(x) dx}. \tag{19}$$

After taking the real part, the particular solution of Eq. (8) now can be expressed as

$$z_1(x, t) = Y_1(x) T_1(t) \frac{A_1(L) z_0}{2\beta_1} \cos\left(\omega_1 t + \frac{\pi}{2}\right) Y_1(x). \tag{20}$$

The amplitude of the deflection of the beam at $x=L$ in the z -direction is denoted as $\delta_{1,\max}$ and given by

$$\delta_{1,\max} \equiv z(L, \omega_1) = \frac{A_1(L) z_0}{2\beta_1} Y_1(L) = \frac{A_1(L) G}{2\omega_1^2 \beta_1} Y_1(L), \tag{21}$$

where $G = z_0(\omega_1)^2$ and $Y_1(L)$

$$= \sqrt{\frac{1}{mL}} \frac{2[\cos(k_1 L) \sin h(k_1 L) - \cos h(k_1 L) \sin(k_1 L)]}{\sin(k_1 L) + \sin h(k_1 L)}. \tag{22}$$

2.3. Electric voltage generation

The z -component of the electrical field displacement vector D_3 for a piezoelectric material may be expressed as [23]:

$$D_3 = d_{31} E_p \left(\frac{\partial^2 z(x, t)}{\partial x^2} (z_N - z_p) \right). \tag{23}$$

Applying Gauss' law to an enclosed rectangular volume across the piezoelectric film of thickness t_p and Young's modulus E_p , the total strain-induced charge Q on the top of the piezoelectric film can be obtained as

$$Q = \int_0^L D_3 w dx = \int_0^L d_{31} E_p \left[\frac{\partial^2 z(x, t)}{\partial x^2} (z_N - z_p) \right] w dx. \tag{24}$$

The induced open-potential between the top and bottom surfaces can be calculated from

$$V = \frac{Q}{C_p} = \left(\frac{t_p d_{31} E_p}{\varepsilon_0 K_p L} \right) \left[(z_N - z_p) \int_0^L \frac{\partial^2 z(x, t)}{\partial x^2} dx \right], \tag{25}$$

where C_p is the piezoelectric layer's capacitance, and is given by $C_p = \varepsilon_0 K_p L w / t_p$.

Since only $n=1$ mode is relevant to our case, Eq. (24) becomes

$$\begin{aligned} Q_1 &= \int_0^L D_3 w dx = \left\{ \int_0^L d_{31} E_p \left[\frac{\partial^2 Y_1(x)}{\partial x^2} (z_N - z_p) \right] w dx \right\} \\ &\times \frac{A_1(L) G}{2\beta_1 \omega_1^2} \cos\left(\omega_1 t + \frac{\pi}{2}\right), \end{aligned} \tag{26}$$

and its amplitude Q_{10} and corresponding voltage amplitude V_{10} may be calculated as

$$Q_{10} = 2k_1 w d_{31} E_p \left(\frac{A_1(L) G}{2\beta_1 \omega_1^2} \right) F_1(L) (z_N - z_p), \tag{27}$$

$$V_{10} = \frac{Q_{10}}{C_p} = 2k_1 \frac{t_p d_{31} E_p}{\varepsilon_0 K_p L} (z_N - z_p) \left(\frac{A_1(L) G}{2\beta_1 \omega_1^2} \right) F_1(L), \tag{28}$$

where

$$F_1(L) = \left(\frac{1}{2k_1} \right) \int_0^L \frac{\partial^2 Y_1(x)}{\partial x^2} dx = \sqrt{\frac{1}{mL}} \frac{\sin(k_1 L) \sin h(k_1 L)}{\sin(k_1 L) + \sin h(k_1 L)} \tag{30}$$

Noting $\delta_{1,\max} = A_1(L) G Y_1(L) / 2\omega_1^2 \beta_1$ and $k_1^2 = w_1 \sqrt{m/EI}$, the voltage amplitude generated can also be put in the form

$$\begin{aligned} V_{10} &= 2k_1 \delta_{1,\max} \frac{t_p d_{31} E_p}{\varepsilon_0 K_p L} (z_N - z_p) \left[\frac{F_1(L)}{Y_1(L)} \right] \\ &= 2(\omega_1)^{1/2} \left[\frac{m}{EI} \right]^{1/4} \delta_{1,\max} \frac{t_p d_{31} E_p}{\varepsilon_0 K_p L} (z_N - z_p) \left[\frac{F_1(L)}{Y_1(L)} \right]. \end{aligned} \tag{31}$$

Table 1

Computational results of resonance frequencies f_c and f_1 , peak voltage output (V_p), peak electric power (P_p), maximum deflection ($\delta_{1,\max}$) with mass-loading (dimensionless damping, $\beta_1 = 0.020$).

Device #	Dimensions $L_{\text{eff}} \times w$ (mm ²)	M (mg)	M/m_b	f_1 (Hz)	f_c (Hz)	$(f_c - f_1)/f_1$ (%)	G (g)	V_p (V)	P_p (μ W)	$\delta_{1,\max}$ (mm)
H1	4.0 × 7.8	28.9	44.9	105.0	105.5	0.4	0.5	1.04	12.8	0.5
							0.7	1.46	25.1	0.6
							1.0	2.09	51.2	0.9
H2	5.0 × 7.8	28.9	31.7	74.7	75.1	0.5	0.5	1.31	20.3	0.9
							0.7	1.84	39.8	1.2
							1.0	2.63	81.3	1.8
H3	6.0 × 7.8	28.9	24.6	56.6	57.0	0.5	0.5	1.59	29.7	1.5
							0.7	2.22	58.2	2.2
							1.0	3.18	119	3.1

Note: experimental values for H3 @ 0.5 g, $V_p = 1.65$ V; $P_p = 32$ μ W, @ 0.7 g, $V_p = 2.31$ V and $P_p = 63$ μ W; @ 1.0 g, $V_p = 3.23$ V and $P_p = 128$ μ W.

Therefore to increase V_{10} , one may increase the maximum deflection $\delta_{1,\max}$; it may be achieved by increasing G (acceleration of the base). Yet, over deflection can cause cantilever fatigue, and fracture in the worst case. So taking into account the yield strength of the cantilever materials one can optimize V_{10} without creating a reliability issue.

2.4. Energy and power generation

The peak energy E_{10} stored in the piezoelectric capacitor for the fundamental mode equal to

$$E_{10} = \frac{C_p}{2} V_{10}^2 = \frac{Q_{10}^2}{2C_p} = 4 \left(\frac{\omega_1 w t_p d_{31}^2 E_p^2}{\epsilon_0 K_p L} \right) \times \sqrt{\frac{m}{EI}} (z_N - z_p)^2 \delta_{1,\max}^2 \left(\frac{F_1(L)}{Y_1(L)} \right)^2. \quad (32)$$

So maximization of E_{10} can be achieved through the maximization of the total charge Q_{10} and minimization of C_p . This simple yet important concept is critical in the design of the PZEH device. So one must increase the maximum deflection $\delta_{1,\max}$, maximizing strain to maximize Q_{10} , and at the same time make the capacitance as small as possible.

Noting that V_{10} is the open-circuit voltage amplitude for $n = 1$ mode. In a real situation it will be connected to a load. Thus, the output power is load-dependent. If one assumes the internal impedance R_i is a function of the internal resistance and capacitance $Z_c = 1/C_p \omega_1$ of the harvester and the resistance dominates, the optimum power output can be achieved by matching the load impedance with R_i . Hence, the maximum output voltage amplitude V_p and output power amplitude P_p can be estimated by

$$V_p = \left[\frac{V_{10} R_i}{(2R_i)} \right] = \frac{V_{10}}{2}; \quad P_p = \left[\frac{V_{10}}{(2R_i)} \right]^2 R_i = \frac{(V_{10})^2}{(4R_i)} \quad (33)$$

where V_{10} is given by Eq. (31).

2.5. Computational calculations

Numerical calculations are performed to calculate the eigenvalues of k_n . It should be reminded that the solution described by Eq. (13) has already satisfied the boundary conditions at $x = 0$. To satisfy the boundary conditions at $x = L$, Eq. (13) is substituted into, Eqs. (11) and (12). Thus, k_n can be determined from finding the roots of $U(L, k_n, t) = 0$,

$$\text{where } U(L, k_n, t) = EI \frac{d^3 z_n(x)}{dx^3} - M \frac{d^2 z_n(x)}{dx^2} \Big|_{x=L}. \quad (34)$$

Specifically, for the excitation of n th mode, noting that

$$z_n(x, t) = \left\{ \frac{A_n(L) z_0 \omega^2}{[(\omega_n^2 - \omega^2)^2 + (2\beta_n \omega_n \omega)^2]^{1/2}} \right\} \times \left\{ [\cos(k_n x) + \cos h(k_n x)] - \frac{\cos(k_n L) + \cos h(k_n L)}{\sin(k_n L) + \sin h(k_n L)} \right. \\ \left. \times [\sin(k_n x) - \sin h(k_n x)] \right\} \left\{ \cos(\omega_n t + \varphi_n) \right\} \quad (35)$$

where

$$\omega_n = k_n^2 \sqrt{\frac{EI}{m}}, \quad f_n = \frac{k_n^2}{2\pi} \sqrt{\frac{EI}{m}}, \quad (36)$$

Meanwhile, the lumped-element model predicts the resonance frequency $f_c = 1/2\pi \sqrt{k_s/M}$, where k_s is called the effective stiffness which is given by Ref. [24]

$$k_s = \frac{3EI}{L^3}. \quad (37)$$

The values of resonance frequency f_c are calculated and listed in Table 1 for comparison to the resonance frequency of the fundamental mode f_1 .

The structure of the harvester is shown in Figs. 3 and 4. It is evident that the dimension along x -direction of the proof mass, L_p , in addition of L , also plays a role of the stiffness of the harvester. In the computations, we introduced the concept of an effective beam length L_{eff} , which is a function of L as well as L_p . The value of L_{eff} and β are determined by fitting the experimentally measured resonance frequencies to theoretical value of f_1 and f_c . Fig. 5 illustrates the best-fitting. The solid-line, the symbol "o" and points with errors (mean \pm error) represent f_c , f_1 and experimental results versus L_{eff} respectively. The best fit gives the following: $L_{\text{eff}} = L + 0.4L_p$ instead of $L_{\text{eff}} = L + 0.5L_p$, which normally would be used. The reason for that may be related to the specific structure of the multi-morph

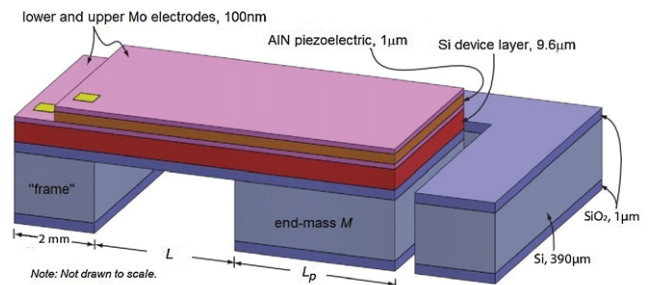


Fig. 3. Illustration of the structure of a monomorph (single piezoelectric layer with two electrodes) PZEH cantilever with a proof mass.

cantilever prepared by MEMS processing (Fig. 4). Fig. 5 also suggests that in the range of resonance frequencies, the predictions of resonance frequency f_c by lumped-element model match those of the solutions of the PDE very well; the disparity is less than 0.5%. Table 1 is a summary of the computational results of multi-morph cantilevers whose structure is shown in Fig. 3 and the acceleration amplitudes of external continuous sinusoidal excitation $G = z_0 \omega_1^2 = 0.5g = 0.5g \cong 5.0 \text{ m/s}^2$, $0.7g \cong 7.0 \text{ m/s}^2$ and $1.0g \cong 10 \text{ m/s}^2$ respectively. The physical parameters used in calculation are listed in Table 2. In computations, in all equations (e.g. Eqs. (19)–(22),

Table 2
Physical parameters used in calculations.

	Si	SiO _x	Mo	AlN			
$E \text{ (N/m}^2\text{)}$	1.60×10^{11}	7.5×10^{10}	3.10×10^{11}	3.05×10^{11}			
$\rho \text{ (kg/m}^3\text{)}$	2330	2200	10200	3260			
K_p	N/A	N/A	N/A	8.9			
Thickness (μm)	$t_1 \text{ SiO}_x$	$t_2 \text{ Si}$	$t_3 \text{ SiO}_x$	$t_4 \text{ Mo}$	$t_5 \text{ AlN}$	$t_6 \text{ Mo}$	$t_7 \text{ SiO}_x$
	1.0	9.6	1.0	0.1	1.0	0.1	1.1

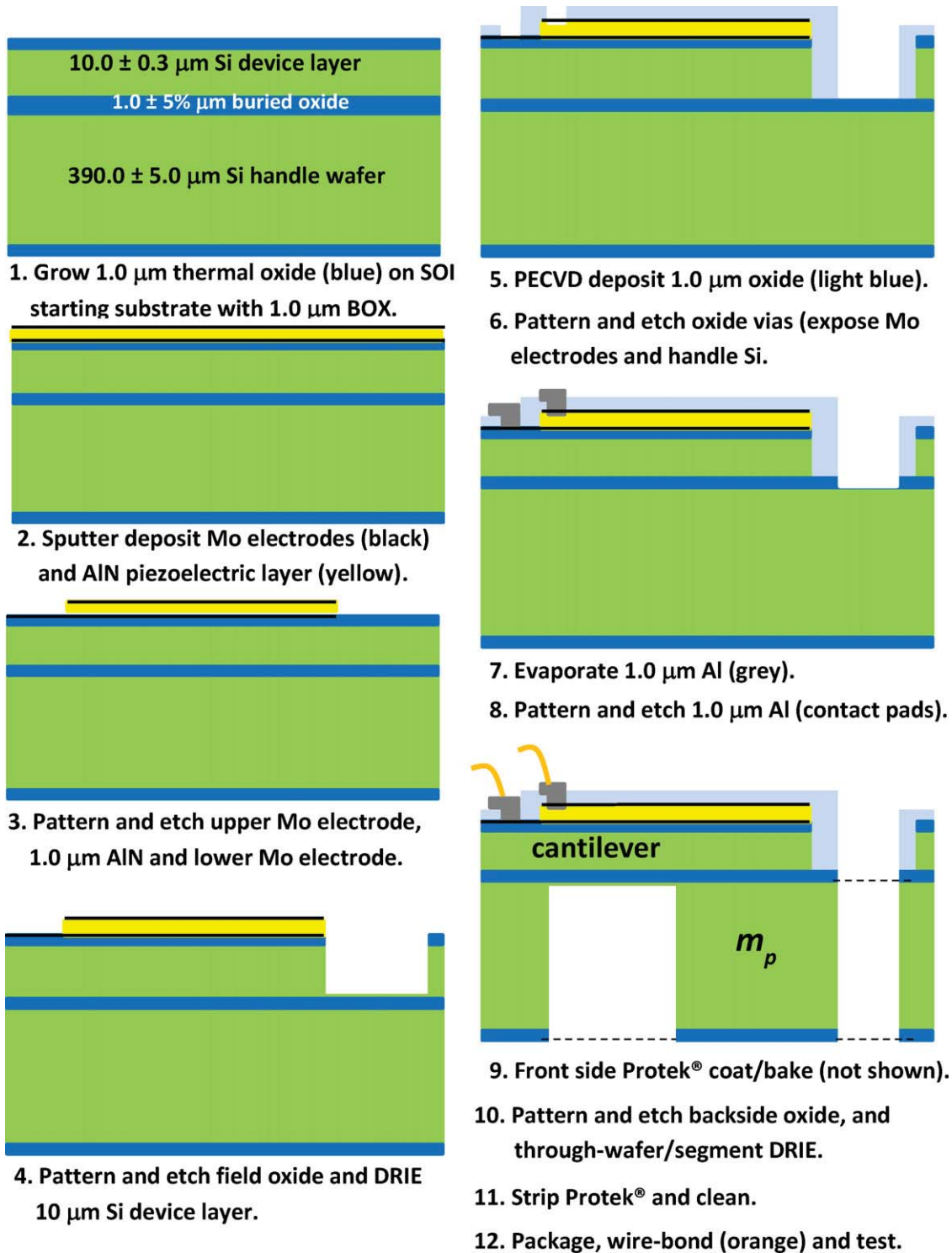


Fig. 4. MEMS AlN-based monomorph (single piezoelectric layer and two electrodes) PZEH fabrication sequence. Not drawn to scale.

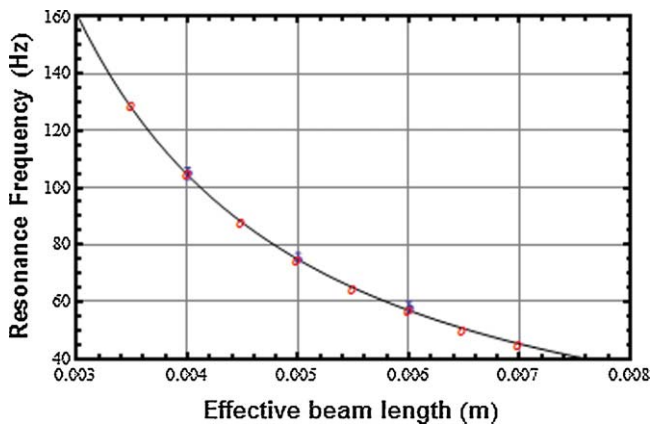


Fig. 5. Fitting experimental results (mean \pm standard deviations of three (3) trials) of resonance frequencies to predictions of f_1 , f_c by PDE model ("o") and lumped-element model (solid curve) respectively with $\beta=0.02$.

(30), (34)–(37)) related to the mechanical properties of the devise, L_{eff} instead of L is used, and in all equations (e.g. Eqs. (24)–(26)) related to electrical properties, L is used.

It should be noted that the distributed parametric model can predict resonance frequencies of other flexural modes which can propagate in a cantilever in addition to the fundamental mode while the lumped-element model only predicts the fundamental frequency f_c ; its counterpart is the first mode f_1 in a distributed system. From the results one may conclude the most effective way

to adjust the working resonance frequency of an energy harvester is to change the loading mass M/m_b ; increase of M/m_b not only decreases f_1 but also increases the output peak voltage V_{10} under the same excitation of G since V_{10} is proportional to $\delta_{1\text{max}}\omega_1 = A_1(L)GY_1(L)/2\omega_1^2\beta_1\sqrt{\omega_1}\sim 1/\omega_1^{3/2}$; it, in turn, enhances the optimum power output amplitude P_{10} . Without the attached loading mass M , it is unrealistic if not impossible to produce a MEMS harvester responding to frequency below 200 Hz.

3. Experiments

3.1. Piezoelectric material selection

Table 3 shows several piezoelectric materials that could be chosen for the PZEH design. The first that comes to mind is the standard lead–zirconate–titanate (PZT). Compared with other piezoelectric materials such as aluminum nitride (AlN) and zinc oxide (ZnO) thin films, there are several issues with fabrication using PZT. For example, there are three (3) elemental constituents in PZT that must be controlled in sputtering to form a film, which makes it rather difficult.

One element in PZT is lead, which may cause hazard to the environment. The European Union's Restrictions of hazardous substance (RoHS) restricts the use of lead in electronics [36]. Therefore, this restricts the market landscape for PZT-based PZEH devices.

Table 3 shows that when taking the material coefficients for V from Eqs. (31) and (33) comparing the calculated values of the other piezoelectric materials to sol–gel PZT, two (2) other

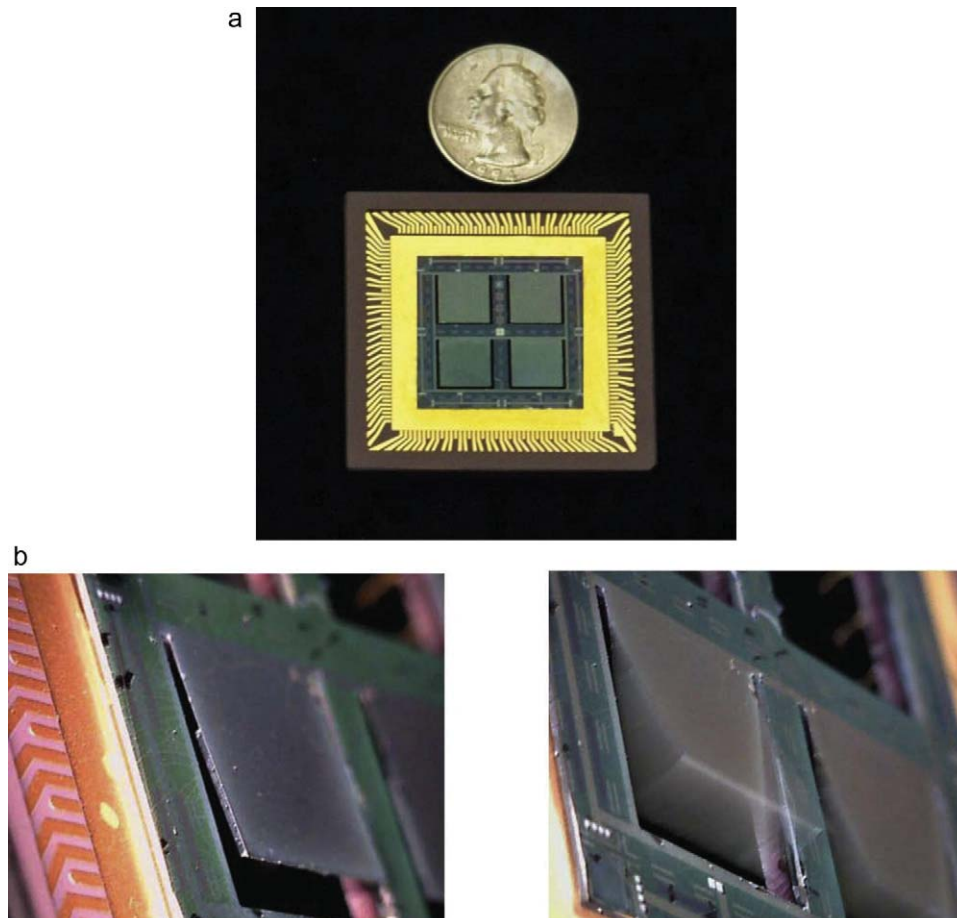


Fig. 6. Actual MEMS-based PZEH, Harvester 3, (a) static position and (b) vibrating at 58 Hz @ 0.5 g (video link: <http://www.youtube.com/watch?v=8-ICU-70M7s>; shown with yellow strobe light).

Table 3
Piezoelectric material comparison for PZEH design.

Material	Piezoelectric coupling coefficient (pC/N) d_{31}	Young's modulus (GPa) E_p	Dielectric constant K_p	Density (g/cc) ρ	Voltage material coefficients* $ (d_{31}(E_p)^{3/4}/K_p)\rho^{1/4} $	Power material coefficients** $[(d_{31}^2(E_p)^{3/2}/K_p^2)\rho^{1/2}]$
Sol-gel lead zirconatetitanate (sol-gel PZT)	-44	100	1700	7.55	1.00	1.00
Single crystal barium titanate (BaTiO3)	-34.5	67	10000	6.02	0.09	0.01
Polyvinylidene fluoride (PVDF)	20	3	12	1.78	1.85	3.41
Lithium niobate (LiNbO3)	-1	181.6	29	4.644	3.23	10.46
Aluminum nitride (AlN)	-2	340	9	3.26	17.43	303.68
Zinc oxide (ZnO)	-5.43	124	10.5	5.68	21.87	478.13

* Normalized to PZT.
** 1st order approximation.

materials emerge; AlN and ZnO are strong alternatives. AlN has already been widely used in the MEMS, microelectronic and micro-sensor industries. ZnO is the other possible candidate to be used in their MEMS-based PZEH design.

3.2. MEMS microfabrication

The MEMS-based fixed-free cantilever PZEH was fabricated using the facility at the Cornell NanoScale Science and Technology Facility in Ithaca, NY. This is a “pure-play” MEMS device, where all materials used are complementary metal-oxide-semiconductor (CMOS) microelectronics compatible. All fabrication was completed on the standard semiconductor fabrication equipment.

The overall MEMS fabrication process is shown in Fig. 4. We started with a p-type 100 mm diameter, double-sided-polished (DSP), (100) CZ silicon (Si) of resistivity 10–20 Ω cm silicon-on-insulator (SOI) wafer. The overall substrate thickness was 400.0 ± 5.0 μm with a within wafer total-thickness-variation (TTV) of less than 1.5 μm. An SOI wafer is two Si wafers fusion bonded together at approximately 1100 °C without interfacial voids with a 1.0 ± 0.05 μm thermal buried oxide (BOX; SiO₂) in between. The top wafer was ground and polished down to 10.0 μm thick with a within-wafer TTV of less than 0.6 μm; this is called the “device layer”, and the bottom wafer is the “handle”. Subsequently, a 1.0 ± 0.05 μm wet thermal SiO₂ (TOX) was grown on both sides of the SOI wafer.

The next step in the process was to perform a full RCA clean [25], and then sputter deposit a stack of 30 nm aluminum nitride (AlN; bottom; adhesion layer), 100 nm molybdenum (Mo; bottom

electrode), 1.0 μm AlN (crystalline piezoelectric material), and 100 nm Mo (top electrode). All thin-film layers were deposited sequentially in situ within a dual chamber of the Tegal sputtering system.

A step-by-step series of photolithography steps and etch steps were performed forming the upper and lower Mo electrodes, which were on top of the fixed-free cantilever. The Mo was etched in a reactive-ion-etch (RIE) system, and the AlN was etched using hot phosphoric acid (both piezoelectric and adhesion layers).

It was then followed by forming a 500 μm wide channel on three sides of the cantilever. This included patterning and etching the 1.0 μm TOX, 10 μm device layer, and 1.0 μm BOX. The thermal oxide layers were etched in an RIE, and the Si was etched using a deep-RIE (DRIE) selectively stopping on the BOX.

A 1.0 μm top layer of plasma-enhanced-chemical-vapor-deposited (PECVD) silicon oxide SiO_x (POX) was deposited under compressive stress. This serves two purposes, (1) to provide a stress compensating layer to the tensile stressed AlN/Mo stack, and (2) to provide passivation. Subsequently, 200 μm × 200 μm square holes are RIE etched into the POX to form via down to the upper and lower Mo electrodes for electrical connections. This must be done with accuracy of the POX wall angle (60°), such that the subsequent evaporated 300 μm × 300 μm aluminum (Al) pads have good step-coverage down to the Mo electrodes. In addition, the Mo electrodes must not be etched away.

The last step was to perform front-to-backside alignment of the backside via. This is an open area, which forms the Si end-mass (proof-mass) on the bottom of the free-end of the cantilever, and mostly release the cantilever. This was completed by first coating the front-side with a spin-on material called ProTEK® SR [26], which was used for through-wafer DRIE with helium (He) backside cooling. The backside TOX was etched using RIE, and the Si was etched through the wafer stopping on the BOX on the bottom of the cantilever, and the surrounding ProTEK® SR [25]. It was also chosen to form DRIE segmentation lines around the perimeter of the die, which were etched simultaneously and allow segmenting the formed die post final release. The final overall cantilever thickness was 13.9 μm, and the end-mass thickness was 390 μm. The overall device cross-section can be seen in Figs. 3 and 4.

Final cantilever release was completed in ProTEK® Remover 100 [27], which is solvent-based. The individual PZEH die was subsequently cleaned in isopropyl alcohol (IPA), and deionized (DI) water, and then dried in air. The die was then plasma cleaned in a YES oxygen asher. Afterwards, the individual die was mounted to a ceramic package, re-ashed, and wire-bonded. The MEMS-based PZEH die was then electrically tested.

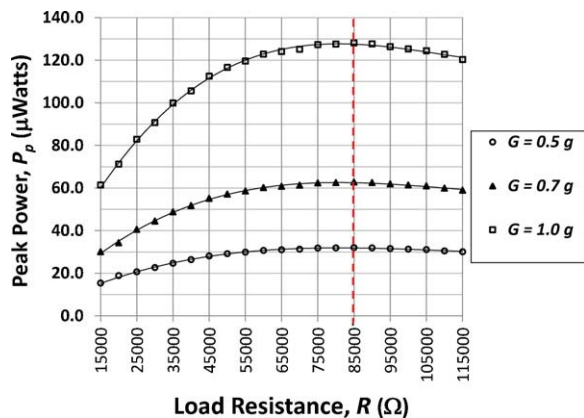


Fig. 7. Plot of peak output power P versus impedance of load R for Harvest 3. Three (3) cases are shown, (1) “o” $G=0.5$ g, (2) “▲” $G=0.7$ g and (3) “■” $G=1.0$ g. Dots are experimental data and the solid curve is the best fit of the function $P = [(V_{10})/(R_i + R)]^2 R$, where R_i is the internal impedance of the harvester. It can be shown that $dP/dR=0$ when $R=R_i$. Thus $P \rightarrow P_p = (V_{10})^2/(4R_i)$ when $R=R_i$. Both P_p and R_i are determined by the best fit curve.

3.3. Testing

There were three types of devices fabricated all with the same cantilever width $W=7.8$ mm, $L_p=4$ mm, $L=4.375, 3.375, 2.375$ mm

and $L_{\text{eff}} = 6.0, 5.0$ and 4.0 mm (Fig. 3). The end-mass has the same mass of 28.9 mg. The measured fundamental resonance frequencies were 58 ± 2 Hz, 75 ± 2 and $105 \text{ Hz} \pm 2$ respectively. The computed resonance frequencies are 56.0 Hz, and 74.7 Hz, 105.0 Hz respectively (Fig. 6). The agreement is good; the error is $<4\%$ (Table 1).

The devices were tested in air with a crude package surrounding the device. The upper and lower see-through covers allowed the cantilever to freely move with millimeters of travel without obstruction. Hence, squeezed-film damping is not a serious factor for consideration until the package becomes smaller.

The optimum power was determined by connecting a variable resistor (R) in series with the harvester in testing. The output power $P = [(V_p)/(R_i + R)]^2 R$, where R_i is the internal impedance of the harvester (Fig. 7). It can be shown that $dP/dR = 0$ when $R = R_i$. Thus $P \rightarrow P_p = (V_{10})^2 / (4R_i)$ when $R = R_i$, where V_{10} is the open peak voltage when $R \rightarrow \infty$. For Harvester 3 the measured R_i is 82.6 k Ω mechanical resonant frequency $f_1 = 58$ Hz with a piezoelectric capacitance $C_p = 3325$ pF. This was measured using a Wavetec model 185 signal generator and a voltage-to-current converter consisting of an LM356 op-amp and a 1 M Ω feedback resistor. Three cases are shown for Harvester 3, (1) $G = 0.5$ g ($g = 9.81 \text{ m/s}^2$), (2) $G = 0.7$ g, and (3) $G = 1.0$ g. The corresponding measured V_p/P_p of the three (3) aforementioned cases are 1.7/32, 2.3/63 and 3.2/128 V/ μ W, respectively. The values of V_p and P_p are in good agreement with the theoretical calculations (disparity $<3.0\%$ and 4% for V_p and P_p respectively) and they are proportional to G and G^2 , respectively as theory predicts. The measured R_i is measured to be 85.0 k Ω consistent with the aforementioned measured value. These devices were all subjected to vibration of 58 Hz and 0.7 g for several days with no degradation of output V_p/P_p , and no changes to the resonant frequency were observed.

We also combined Harvester 3 with the THINERGY[®] IPS-EVAL-EH-01 Energy Harvesting Evaluation Kit provided by Infinite Power Solutions (IPS; www.infinitepowersolutions.com) to power-up a complete self-powered wireless sensor (WS) node (see Fig. 8). The IPS-EVAL-EH-01 is a universal energy harvesting evaluation kit that accepts energy from a variety of energy harvesting transducers (both alternating current (AC) and direct current (DC) voltage sources), and efficiently stores the energy in a THINERGY[®] MEC101 solid-state micro-energy cell (MEC), a unique thin-film battery with the size of a postage stamp. The IPS THINERGY MEC101 is a near loss-less energy storage device which is able to accept charge currents less than 1 μ A making it ideal for energy harvesting applications. The energy conversion efficiency from the PZEH device to the MEC101 was not measured. This is IPS proprietary information, yet it can be said that it depends on several factors (PZEH impedance, level of input current, and temperature), and can be as high as 85%.

The IPS-EVAL-EH-01 kit also included the MAX17710 energy harvesting power management integrated circuit (PMIC) from maxim integrated products (www.maxim-ic.com) which provides an input voltage boost circuit if needed (if $V_{\text{load}} \leq 2$ V), manages the charge of the battery and provides a programmable regulated output voltage to power the load. For this demonstration, the popular ez430-RF2500 wireless temperature sensor demo from Texas Instruments' (www.ti.com) was used as the load, which features an integrated MSP430 microcontroller and CC2500 2.4 GHz radio transceivers to transmit temperature data.

This demonstration was completed in June at the 2011 Sensors Expo and Conference held in Chicago, IL [27]. Prior to the demonstration the MEC101 was discharged. The shaker input excitation was set to 58 Hz with acceleration amplitude of 0.7 g corresponding to V_p of 2.3 V (loaded approximately 1.4 V; hence the internal voltage boost of the IPS-EVAL-EH-01 was more than likely utilized), and P_p of 63 μ W. Approximately <20 s after the shaker was turned on the IPS-EVAL-EH-01 wireless signal was detected. This successful

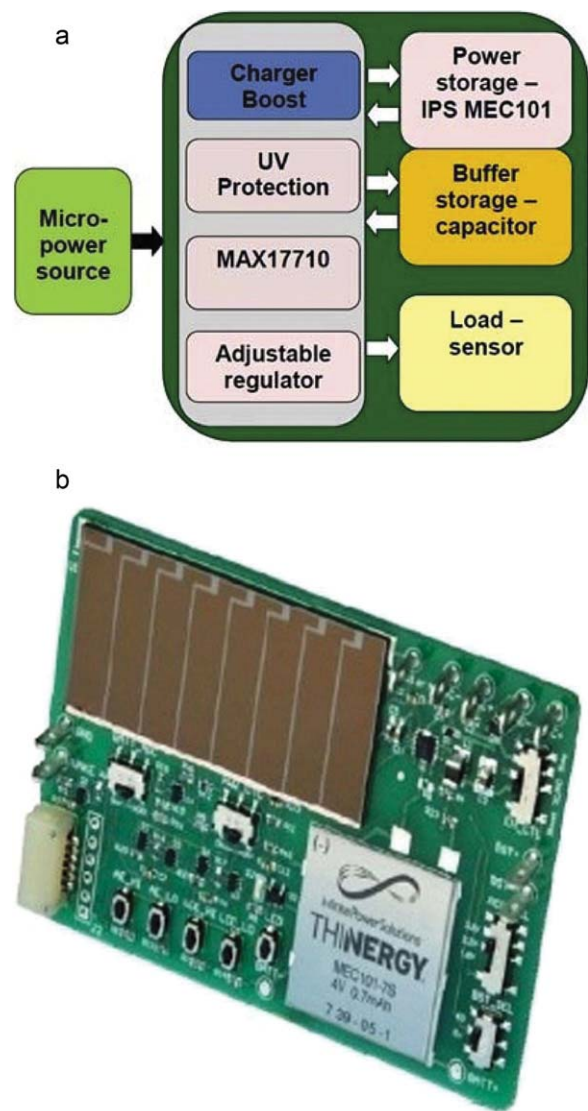


Fig. 8. THINERGY[®] IPS-EVAL-EH-01 energy harvesting evaluation kit with MEC101 advanced solid-state thin-film battery for power storage, (a) and its associated circuit (b).

WS node demonstration was completed at vibration levels that correspond to a typical United States (US) industrial environment with 60 Hz AC electricity providing power for various items of equipment (e.g. pumps, fans) that are desired to be monitored for condition.

4. Performance comparison

It should be noted that as a practical matter most wireless sensor and WSN applications have $G = 0.6 \pm 0.3$ g acceleration levels [4]. Some may have more (e.g. automobile engine block, shock in tires) and many others have less (e.g. the Mackinac Bridge in Michigan vibrates at 100–105 Hz with <0.1 g acceleration while automobiles drive over it) [28,29]. Secondly, typical vibration sources may have resonance frequencies <250 Hz. Industrial applications vibrate at 60 Hz and 50 Hz and at higher harmonics in the US and European Union (EU)/Asia, respectively. So, it is very important to know the environment for which the PZEH device is designed.

Table 4 shows a few examples of recently reported modest to high power (relatively speaking; $>100 \mu$ W per device) MEMS-based PZEH devices [17,30–35]. Although several researchers have shown

Table 4
MEMS-based PZEH performance comparison.

Institution (s)	MEMS device type (<i>v</i> [cm ³])	Material	Resonant frequency, <i>f</i> ₁ (Hz)	Bandwidth, Δ <i>f</i> ₁ (Hz)	Acceleration, <i>G</i> (g)	Peak voltage, <i>V</i> (V)	Power, <i>P</i> (μW)	Figure of Merit (μW/cm ³ /g ²)	Date	Ref.
Ideal device	Any (≤1 cm ³)	RoHS compliant (no lead) ^y	≤250	≤2	≤0.50	≥2.0 ^d	≥100 ^d	≥2.00 ^d	n/a	n/a
IMEC-Holst	Fixed-free monomorph (~2 cm ³)	PZT	1800	~2	2.50	Not stated	40	0.00	2007	[30]
IMEC-Holst	Fixed-free monomorph (~2 cm ³)	AlN	572	~2	2.00	Not stated	60	0.03	2008	[30]
IMEC-Holst	Fixed-free monomorph (~2 cm ³)	AlN	352	~2	1.75	Not stated	85	0.08	2009	[31]
IMEC-Holst	Fixed-free monomorph (~2 cm ³)	AlN	572	~2	1.00	Not stated	100	0.17	2009	[32]
IMEC-Holst	Fixed-free monomorph (~2 cm ³)	AlN	929	~2	2.50	Not stated	225	0.04	2010	[33]
IMEC-Holst	Fixed-free monomorph (~2 cm ³)	AlN	1011	~2	4.50	Not stated	489	0.02	2011	[34]
UVM/Cornell	Fixed-free monomorph (~3 cm ³ ^e)	AlN	58	~2	0.50	1.7	32	1.43	2011	[27]
UVM/Cornell	Fixed-free monomorph (~3 cm ³ ^e)	AlN	58	~2	0.70	2.3	63	1.43	2011	[27]
UVM/Cornell	Fixed-free monomorph (~3 cm ³ ^e)	AlN	58	~2	1.00	3.2	128	1.43	2011	[27]
UMichigan	Fixed-free monomorph (~2 cm ³)	PZT	154 ^a	14 ^a	1.50	4.3	205	4.14 ^a	2011	[35]
MIT	Fixed-free monomorph (~4 cm ²)	PZT	1300 ^a	~400 ^a	Not stated ^b	0.8	45	6.92 ^a	2011	[17]

^a Broadband designs; all others are high-Q designs.

^b Assumes *G* = 1.0 g.

^c [36].

^d Based upon typical wireless sensor nodes requiring minimum of 2.0 V and 100 μW.

^e Currently packaged in standard off-the-shelf integrated circuit package; moving to wafer-level-packaging (WLP) to reduce form-factor.

some noteworthy results, it is clear to the authors that no previous MEMS PZEH device has ever been within the aforementioned ranges for output voltage *V* and power *P* with applicable vibration levels at low frequencies <100 Hz and acceleration <1.0 g until now.

A parameter, “Figure of Merit (*F.O.M.*)”, has been used to evaluated the performance of a harvester [35], which is defined by the power density per *G*² multiplied by the ratio of the bandwidth to resonant frequency (Δ*f*₁/*f*₁)

$$F.O.M \equiv \left(\frac{P_p}{vG^2} \right) \left(\frac{\Delta f_1}{f_1} \right) \tag{38}$$

where *v* is the volume of the fully packaged PZEH device. For a high-*Q_f* resonant device the typical Δ*f*₁ is on the order of 2 Hz (in air with no squeeze-film damping), or less depending upon vacuum packaging level. Using the aforementioned parameters defined prior for a typical wireless sensor in a typical vibrational environment then *F.O.M.* must be ≤2 μWs/cm³/g² for a high-*Q_f* resonator. As shown in Table 4 the test results of *F.O.M.* reported in this paper have the highest *F.O.M.* compared to other investigations testing results of the similar devices.

It should be pointed out that PZEH devices designed with broad bandwidth would have greater Δ*f*₁ and thus greater *F.O.M.* However, absolute *P* must be increased to compensate. Hence, the research results from MIT and the University of Michigan are noteworthy since these are broad bandwidth PZEH designs. [17,35] Broadband designs are of keen interest and should be strongly considered since wider bandwidth will help with temperature dependence for the given environmental conditions (e.g. wide temperature range of TPMS). Yet, MIT’s design has too high resonant frequency with only modest *P*, and University of Michigan’s investigators uses too high acceleration excitation (resulting in higher *P*) for typical wireless sensor application conditions.

5. Conclusion

This work has shown that it is possible to accurately predict the behavior of MEMS-based PZEH devices prior to their manufacture. In addition, it has been shown that relevant low frequency and low *G*-force acceleration levels of an AlN-based MEMS PZEH device can provide enough *V* and *P* to enable low power electronic systems, such as wireless sensors.

Funding sources

This project was partially funded by the HAS Fund of Physics Department, University of Vermont (UVM; www.uvm.edu), by the UVM Pre-Seed and Innovations Funds, by a NASA/VT EPSCoR Phase (0) SBIR grant, and by a NY State Energy Research and Development Authority (NYSERDA; www.nysesda.org) contract. This work was performed in part at the Cornell NanoScale Science and Technology Facility (CNF; www.cnf.cornell.edu), a member of the National Nanotechnology Infrastructure Network (NNIN), which is supported by the National Science Foundation (grant ECS-0335765). In addition, this work was partially funded by the Cornell University Energy Materials Center (EMC2; www.emc2.cornell.edu), which is supported in part by the Department of Energy (DoE; www.eere.energy.gov), and the NY State Foundation for Science, Technology and Innovation (NYSTAR; www.nystar.state.ny.us).

References

[1] R. Andosca, K. Lee, J. Wu, Efficient vibrational energy harvesting for WSN applications, in: Invited presentation to the NanoPower Forum Workshop/Darnell Group, San Jose, CA, 2009, pp. 18–20.

- [2] R. Andosca, K. Lee, N. Stoffel, J. Wu, P. Tspelief, M.S. Germaine, MEMS energy harvesting for WSN applications, in: Invited Presentation to the 2009 Sensors Expo and Conference, Rosemont, IL, 2009.
- [3] R.R. Vuellers, Micropower Energy harvesters for autonomous wireless sensor nodes: from lab to reality, in: 2009 Sensors Expo and Conference, Chicago, 2009.
- [4] S. Roundy, P.K. Wright, J. Rabaey, Energy Scavenging for Wireless Sensor Networks with Special Focus on Vibrations, Kluwer Academic Publishers, Boston, 2004.
- [5] R. Quinell, Energy scavenging yields endless power possibilities, *Electron. Des.* (2009) 22.
- [6] E. Halvorsen, Energy harvesters driven by broadband random vibrations, *J. MicroElectroMechan. Syst.* 17 (2008) 1061–1071.
- [7] S.N. Chen, G.J. Wang, M.C. Chien, Analytical modeling of piezoelectric vibration-induced micro power generator, *Mechatronics* 16 (2006) 379–387.
- [8] Y.B. Jeon, R. Sood, J.H. Jeong, S. Kim, MEMS Power generator with transverse mode thin film PZT, *Sens. Actuators A* 122 (2005) 16–22.
- [9] S.W. Arms, C.P. Townsend, D.L. Churchill, J.H. Galbreath, S.W. Mundell, Power Management for energy harvesting wireless sensors, in: Proceedings of SPIE International Symposium on Smart Structures and Smart Materials, San Diego, CA, 2005, pp. 1–9.
- [10] A. Kasyap, A. Phipps, M. Sheplak, K. Ngo, T. Nishida, L. Cattafesta, Lumped element modeling of piezoelectric cantilever beams for vibrational energy reclamation, in: Proceedings of ASME International Mechanical Engineering Congress and Exposition, Chicago, IL, 2006, pp. 1–7.
- [11] S.P. Beeby, M.J. Tudor, N.M. White, Energy harvesting vibration sources for microsystems applications, *Meas. Sci. Technol.* 17 (2006) R175–R195.
- [12] R.G. Andosca, J. Wu, Energy harvesting – power everywhere, in: MIT/Stanford Venture Lab mini-conference, April 19, 2011, <http://www.youtube.com/watch?v=PQyP.J2s6DE>.
- [13] F. Peano, G. Coppa, C. Serazio, F. Peinetti, A. D'angola, Non-linear oscillations in a MEMS energy scavenger, *Math. Comput. Model.* 43 (2006) 1412–1423.
- [14] S.M. Gracewski, P.D. Funkenbusch, Z. Jia, D.S. Ross, M.D. Potter, Design and modeling of a micro-energy harvester using an embedded charge layer, *J. Micromech. Microeng.* 16 (2005) 235–241.
- [15] E. Reilly, E. Carleton, P.K. Wright, Thin film piezoelectric energy scavenging systems for long term medical monitoring, in: The Third International Workshop on Body Sensor Networks. IEEE Conference at MIT Cambridge MA, 2006, pp. 38–41, 0-7695-2547.
- [16] Power-Scavenging Batteries: Inexpensive chips harvest mechanical energy to charge batteries for wireless sensors, August 25, 2011 <http://www.technologyreview.com/energy/38434/?p1=MstRcnt>.
- [17] A. Hajati, S.-G. Kim, Ultra-wide bandwidth piezoelectric energy harvesting, *Appl. Phys. Lett.* 99 (2011) (083105-1-083105-3).
- [18] A. Erturk, D.J. Inman, A distributed parameter electromechanical model for cantilevered piezoelectric energy harvesters, *J. Vib. Acoustics* 130 (2008) (041002-1041002-15).
- [19] L. Meirovitch, *Fundamentals of Vibrations*, McGraw-Hill, New York, 2001.
- [20] M.S. Weinberg, Working equations for piezoelectric actuators and sensors, *JMEMS* V8 N4 (1999) 529–533.
- [21] M.P. Morse, *Vibration and Sound*, McGraw-Hill, New York, 1948.
- [22] K.F. Riley, M.P. Hobson, S.J. Bence, *Mathematical Methods for Physics and Engineering*, Third Edition, Cambridge University Press, 2008.
- [23] B.A. Auld, *Acoustic Fields and Waves in Solids*, vol. I, Second ed., Krieger Publishing Co., Malabar, Florida, 1990.
- [24] C. Liu, *Foundations of MEMS*, Pearson Prentice Hall, Upper Saddle River, NY, 2006.
- [25] RCA Clean, 2011, http://en.wikipedia.org/wiki/RCA_clean.
- [26] ProTEK® SR Coatings for DRIE Processes, 2011, <http://www.brewerscience.com/products/protective-coatings/scratch-resistant-etch-protectivecoating>.
- [27] MicroGen's BOLT™ MEMS Energy harvester combines with infinite power solutions' THINERGY® MEC to Create Self-powered Wireless Sensor Node: MicroGen demonstrates missing-link to efficient and reliable vibrational Energy Harvesting solutions, Chicago, IL (PRWEB) June 21, 2011 <http://www.prweb.com/releases/2011/6/prweb8585499.htm>.
- [28] D.J. Caccamise, M.S. Schenewerk, Whole LottaShakin Goin On, describing some of the results from the Mackinac Bridge monitoring project April 24, 2008, www.pobonline.com.
- [29] D.J. Caccamise, Vibrational frequencies of Mackinac Bridge, 2009 (private conversation).
- [30] R. Vuellers, Energy harvesting for autonomous sensor systems, Holst Centre/IMEC, The Netherlands, 2009, http://www2.fhi.nl/senseofcontact/archieff/2009/images/holst_centre_energy_harvesting_for_autonomous_sensor_nodes_r.vuellers.pdf.
- [31] R. Elfrink, M. Renaud, T.M. Kamel, C. de Nooijer, M. Jambunathan, M. Goedbloed, D. Hohfeld, S. Matova, V. Pop, L. Caballero, R. Schaijk, Vacuum-packaged piezoelectric vibration energy harvesters: damping contributions and autonomy for a wireless sensor system, *J. Micromech. Microeng.* 20 (2010) 1–7, 104001.
- [32] R. Elfrink, V. Pop, D. Hohfeld, T.M. Kamel, S. Matova, C. de Nooijer, M. Jambunathan, M. Goedbloed, L. Caballero, M. Renaud, J. Penders, R. van Schaijk, First autonomous wireless sensor node powered by a vacuum-packaged MEMS energy harvester, in: Electron Devices Meeting (IEDM), IEEE International, 7–9 Dec. 2009, Baltimore, MD, 2009, pp. 1–4.
- [33] Holst Centre/IMEC, The Netherlands: AIN-based MEMS PZEH device, 225 μ W, 929 Hz, 2.5 g 2010, (private conversation).
- [34] R. Elfrink, S. Matova, C. de Nooijer, M. Jambunathan, M. Goedbloed, J. van de Molengraft, V. Pop, R.J.M. Vuellers, M. Renaud, R. van Schaijk, Shock induced energy harvesting with a MEMS harvester for automotive applications, in: Electron Devices Meeting (IEDM), IEEE International, 5–7 Dec. 2011, Washington, D.C., 2011, 29.5.1–29.5.4.
- [35] E.E. Aktakka, R.L. Peterson, K. Najafi, Thinned PZT on SOI process and design optimization for piezoelectric inertial energy harvesting, in: 16th International Conference on Solid-State Sensors, Actuators, and Microsystems, Transducers 2011, Beijing, China, June 2011, 2011, pp. 1649–1652.
- [36] Directive on the restriction of the use of certain hazardous substances in electrical and electronic equipment 2002/95/EC commonly referred to as the Restriction of Hazardous Substances Directive or RoHS was adopted in February 2003 by the European Union, 2011, http://en.wikipedia.org/wiki/Restriction_of_Hazardous_Substances_Directive.

Biographies

Robert Andosca is the Founder, President and CTO of MicroGen Systems, Inc. (www.microgensystems.com, located in Ithaca, NY at the *Cornell Business and Technology Park*. MicroGen, The University of Vermont (UVM; www.uvm.edu) and Cornell University's Energy Materials Center (EMC2; www.emc2.cornell.edu) are developing the patent-pending MicroElectroMechanical Systems (MEMS) based piezoelectric vibrational energy harvester (PZEH) micro-power generator. Mr. Andosca has 20+ years professional experience, which ranges from operational to technical management, business development, and the design and development of MEMS and semiconductor products. He held senior level positions at the Infotonics Technology Center (now called STC MEMS), Lilliputian Systems, Umicore, Corning IntelliSense, Clare Corporation and Lockheed Martin. He is Ph.D. candidate of the Materials Science UVM and expected to obtain the degree in 2012. He holds an M.S. in Materials Science from UVM, and B.S. degrees in Mathematics and Physics from USNH, Keene State College.

T. Gus McDonald has 30+ years' experience in MEMS and photonic research, development, prototyping, manufacturing and business development. Mr. McDonald is currently the Director of Engineering at MicroGen Systems, Inc. Previously, he worked at Texas Instruments (TI; www.ti.com) for 19 years in a variety of positions including as a Member Technical Staff in early development of TI's digital light projection (DLP) deformable mirror display (DMD) MEMS technology. Since leaving TI he has worked at Corning Inc., Kodak-ITT space systems and Infotonics Technology Center (now called STC MEMS). All of these positions involved packaging, assembly and test for a range of technologies including MEMS and liquid crystal based assemblies. He has a B.S. in Physics from the University of Texas, Dallas and has 13 patents.

Vincent Genova since 1999 has been a Research Staff Scientist at the Cornell NanoScale Science and Technology Facility (CNF; www.cnf.cornell.edu) at Cornell University in Ithaca, NY. Mr. Genova is active in process development and technical direction for the atomic layer deposition (ALD) and reactive ion etch (RIE) areas, and assists the facility with projects involving MEMS, CMOS, and III-V based device processing. Prior to joining the CNF Mr. Genova worked in the MEMS, III-V and semiconductor industries. He worked for Eastman Kodak Research Labs, and IBM's Yorktown/East Fishkill Development Laboratory working on numerous technologies, including MEMS and microfluidic devices, flat panel displays, and GaAs-based devices from MESFETs to p-HEMTs. Mr. Genova completed his M. Eng. in Applied Physics at Cornell University in 1983, and his BS in Physics at the State University of New York at Binghamton in 1981. He has co-authored journal articles on ALD, integrated device fabrication and RIE.

Steven Rosenberg is a MEMS Process Development Engineer for MicroGen Systems, Inc. performing microfabrication at the *Cornell NanoScale Science and Technology Facility* (CNF; www.cnf.cornell.edu). Mr. Rosenberg has 20+ years of experience ranging from a novice production worker, and worked hard to become a development engineer. Mr. Rosenberg held positions for Analog Devices, Alpha Industries, Corning IntelliSense, and Qimonda. He completed his ASEE (2010), with a semiconductor specialty, at J. Sargeant Reynolds Community College in Richmond, VA

Joseph Keating studied electrical and computer engineering at The University of Colorado, Boulder (BS, 1990), including graduate level studies in optical-electronics. Mr. Keating began his career as an embedded electronics design engineer. Joe has fifteen years of experience in battery design development and applications support. Currently, Joe is the Director of the Applications Engineer department responsible for developing deeply embedded wireless applications that utilize energy harvesting at Infinite Power Solutions, Inc. (www.infinitepowersolutions.com), in Littleton, Colorado.

Cole Bendixen began working for Infinite Power Solutions (IPS) in 2008 in the Applications Engineering group. During his tenure with IPS, Mr. Bendixen has designed and developed new low-power applications that enable and showcase the IPS product line. Mr. Bendixen earned a BS in Electrical and Computer Engineering from the University of Colorado, Boulder; also completing the Embedded Systems Certificate Program.

Junru Wu received his Ph.D. (1985) and postdoc training (1987) in non-linear acoustics at the University of California at Los Angeles. Currently, Dr. Junru Wu is a tenured full professor of University of Vermont and founder of MicroGen Systems Inc. Dr. Wu was elected as a Fellow of the Acoustical Society of America, the American Institute of Ultrasound in Medicine, and an Elected Life-time-Full Member of Vermont Academy of Science and Engineering. He has received several awards; his contribution to nonlinear acoustics was listed as one of the most

important achievement in Physical Acoustics in “Acoustical Society of America 75th Anniversary Time-Line.” He has been considered one of internationally renowned experts in nonlinear physics, soliton physics, and the biological physics. He has published more than 120 papers in *Physical Review Letter*, the *Journal of Acoustic Society*, *Ultrasound in Medicine and Biology*, the *Physics in Medicine and Biology* and the *Advanced Drug Delivery Reviews*.